Formation of Antihydrogen Rydberg atoms in strong magnetic field traps

T. Pohl and H. R. Sadeghpour

ITAMP, Harvard-Smithsonian Center for Astrophysics, 60 Garden Street, Cambridge MA 02138

Abstract. It is shown that several features of antihydrogen production in nested Penning traps can be described with accurate and efficient Monte Carlo simulations. It is found that cold deeply-bound Rydberg states of antihydrogen ($\bar{\mathrm{H}}$) are produced in three-body capture in the ATRAP experiments and an additional formation mechanism -Rydberg charge transfer-, particular to the nested Penning trap geometry, is responsible for the observed fast (hot) $\bar{\mathrm{H}}$ atoms. Detailed description of the numerical propagation technique for following extreme close encounters is given. An analytic derivation of the power law behavior of the field ionization spectrum is provided.

Keywords: Rydberg antimatter, antihydrogen, non-neutral plasma, three-body capture, charge transfer
PACS: 36.10.-k,34.70.+e,52.20.Hv

I. INTRODUCTION

Since the initial success of the ATHENA [1] and ATRAP [2, 3] collaborations in producing the first neutral form of antimatter (antihydrogen – $\bar{\mathrm{H}}$) in nested Penning traps at CERN, sizable effort has been devoted, both in experiment and in theory, to understanding how these atoms in strong magnetic fields form, how hot (or cold) they are, and what the internal states of such exotic form of matter may be. Subsequent measurements by these groups showed that the produced $\bar{\mathrm{H}}$ atoms are not in thermal equilibrium with the surrounding positron plasma and are hot (fast) atoms [4, 5]. Additionally, ATRAP observations hinted at formation of deeply-bound Rydberg atoms [6]. In the following, we will address in detail, these open questions in $\bar{\mathrm{H}}$ formation in nested Penning traps.

While the numerical simulations have consistently established that the three-body interaction of two positrons (e^+) and an antiproton ($\bar{p}$) in a magnetic field likely forms atoms that are weakly bound [7, 8, 9, 10, 11], a more recent refinement of ATRAP experiments has produced evidence, in the field ionization spectrum, for highly-bound atomic states [6]. The origin and characteristics of such deeply-bound $\bar{\mathrm{H}}$ atoms has only recently been revealed in extensive and precise classical Monte-Carlo simulations of TBC of $\bar{\mathrm{H}}$ atoms [12]. The calculations were conducted on two levels of sophistication. For low- to moderate-fields, at which weakly-bound Rydberg levels are ionized, the guiding-center approximation of an atom in a magnetic field (GCA) was employed, which holds that different degrees of freedom for atomic motion, the cyclotron, magnetron and axial bounce motions, evolve separately in the magnetic field. Since the cyclotron period, $\tau_c = 2\pi m/e$ is the fastest period in the system, followed by the axial bounce period, $\tau_z = 2\pi\sqrt{r_e c^3/\rho^3}$, and the magnetron oscillation period, $\tau_m = (2\pi\omega_c\rho^3)/(r_e c^3)$, the GCA simulations freeze the e^+ cyclotron motion. In the above expressions, e and m are

CP1037, *Cold Antimatter Plasmas and Application to Fundamental Physics*, edited by Y. Kanai and Y. Yamazaki

the charge and the mass in a magnetic field B, r_e and ρ are the classical electron radius and the radial coordinate, assumed to be much larger than the cyclotron radius (circular GCA atom), $r_c = \sqrt{2mk_BT}/(eB)$, and c is the speed of light [13]. Such a picture of strongly-magnetized atoms, breaks down when there is coupling between different degrees of freedom, as for instance, when the atoms are so deeply bound that the Coulomb and magnetic interactions compete *on par*, leading to chaotic electronic motion. In these cases, we employ an efficient and numerically stable regularization scheme in Monte Carlo simulation of TBC for formation of deeply-bound states.

Below, we describe the field ionization of deeply-bound $\bar{\mathrm{H}}$ atoms, and derive an analytic expression for the power-law behavior of surviving atom number with field strength. We will demonstrate the a unique two-step collisional process leads to the formation of such deeply-bound atoms and give a full account of the numerical technique which allows us to account for close binary encounters in the Coulomb field. We account for an additional collision process, which explains the high $\bar{\mathrm{H}}$ axial velocities observed in [4]. This mechanism, the charge exchange of TBC $\bar{\mathrm{H}}$ atoms with $\bar{p}$ ions in the trap, permits the bound e^+ of initially slow $\bar{\mathrm{H}}$ atoms to hop onto the fast $\bar{p}$ ions in the side-wells of the nested Penning trap, thereby producing high velocity $\bar{\mathrm{H}}$ atoms. Detailed comparisons with observations are made.

II. EXPERIMENTAL OBSERVATIONS

A. Plasma confinement and $\bar{\mathrm{H}}$ production

All $\bar{\mathrm{H}}$ production experiments used a nested Penning trap to simultaneously confine e^+ and $\bar{p}$ and to create an overlap region for $\bar{\mathrm{H}}$ formation. A strong homogeneous magnetic field provides confinement of both species radially to the magnetic field axis, while an electrostatic double-well potential axially traps e^+ in the center of the trap and confines $\bar{p}$ in the side-wells.

The ATHENA experiments [1] as well as the initial ATRAP $\bar{\mathrm{H}}$ production scheme [2], were based on injection of energetic $\bar{p}$ which subsequently cooled through collisions with the e^+ . Subsequent ATRAP experiments aimed at optimizing $\bar{\mathrm{H}}$ production, by preparing cold $\bar{p}$ localized in one of the side-wells which were driven through the e^+ cloud by an rf-field. Gentle driving is expected to yield slow $\bar{p}$ in the central reaction region and, hence, to produce slow $\bar{\mathrm{H}}$ atoms. The atoms were detected in an ionization well, located axially outside the trap. Since atoms also drift radially to the magnetic field axis, this methods detects a fraction of the $\bar{\mathrm{H}}$ arriving at the detector within a small solid angle α. This detection scheme, on the other hand, allows for nearly background-free observation of the atoms and has the distinct advantage that pre-ionization fields can be applied to probe internal and translational states of the atoms.

B. Field ionization

In the ATRAP driven experiment [3], a static electric field has been applied in front of the detector that ionizes less deeply bound atoms and prevents them from reaching

the detection well. Through varying the strength of the pre-ionization field, and state selective stripping of the bound e^+, the distribution of internal atomic Rydberg states can be probed. The resulting number of $\bar{H}$ atoms that survive a given electric field, F is shown in Fig. 1. Two main features are evident: (a) at low fields, the surviving atoms follow a simple power-law dependence $N \sim F^{-2}$, and (b) an enhancement of the atom number with respect to this power-law, at larger fields. The origin of both the low-field and the high-field behavior is not immediately obvious, from consideration of either radiative recombination or three-body capture. For example, extrapolating the classical infinite-field calculations [9] overestimates the power-law exponent in the low-field regime [14].

B. Velocity measurement

In 2004, the ATRAP collaboration succeeded in measuring the velocity distribution of such atoms [4]. In this particular experiment, a prestripping oscillating electric field is applied before the detection well, such that the speed of the $\bar{H}$ atoms moving along the magnetic field could be measured by tuning the frequency of the oscillating field.

In arriving at a velocity of the antihydrogen atoms, it was assumed that the number density of observed atoms, with velocity v in an ionizing field F, scaled as $N(v,F) \sim \delta(v - v_0)F^{-3}$. A most probable value of $v_0 = 200$ meV, corresponding to a temperature of $T = 2400$ K, was found to best describe the observed frequency spectrum. This result was a surprise, since the atomic temperature expected from the 4.2 K background temperature is about three orders of magnitude smaller. As we discuss below, an additional mechanism may be at play in forming fast non-thermal $\bar{H}$ from initially slow atoms.

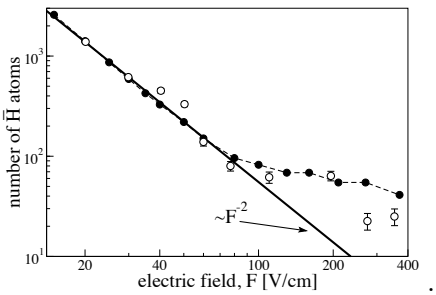

FIGURE 1. Field ionization spectrum of $\bar{H}$ atoms that survive an electric field F. ATRAP measurements [6] (open circles) are compared to exact Monte-Carlo calculations for $kT_{\bar{H}} = 2$ meV (filled circles). The curves have been scaled to experiment at 20 V/cm.

III. CLASSICAL MONTE-CARLO SIMULATIONS

At experimental densities and temperatures, radiative processes and quantum effects are of minor importance, permitting a classical description of $\bar{H}$ through three-body collisions between $\bar{p}$ and e^+. Although a solution of the classical equations of motion for

a two-component plasma system is fairly straightforward, the sheer number of particles ($\sim 10^6$) renders a full scale simulation of the entire trap impractical. However, since $\rho_{\bar{p}}$ in the central trapping region is considerably smaller than the ρ_{e^+}, the $\bar{p}-\bar{p}$ interaction is negligible for the formation process. Exploiting this fact [11, 12], we restrict the simulation to the dynamics of a single $\bar{p}$ traversing the central trap cloud, but repeating the calculations over many cycles. The numerical effort is further reduced by considering e^+ in a finite cubic box, centered around the moving $\bar{p}$. This box is constantly filled with e^+ according to the corresponding equilibrium phase space distribution, with density ρ_{e^+} and temperature T_{e^+}.

After the $\bar{p}$ leave the plasma cloud, the critical ionization field of formed atoms is calculated by slowly ramping up an electric field until a bound e^+ is liberated. Average quantities, such as the corresponding field ionization spectrum are finally calculated from many repetitions of these single $\bar{p}$ simulations. The system is propagated by solving the following classical equations of motion for the $\bar{p}$

$$\dot{\mathbf{R}} = \mathbf{V}\,, M\dot{\mathbf{V}} = \mathbf{F} - m\boldsymbol{\omega}_{\mathrm{c}} \times \mathbf{V} \tag{1}$$

and the e^+ s

$$\dot{\mathbf{r}}^{(i)} = \mathbf{v}^{(i)}\,, \quad m\dot{\mathbf{v}}^{(i)} = \mathbf{f}^{(i)} + m\boldsymbol{\omega}_{\mathrm{c}} \times \mathbf{v}^{(i)}\,, \tag{2}$$

where $\boldsymbol{\omega}_{\mathrm{c}} = (0,0,\omega_{\mathrm{c}})$ is the e^+ cyclotron frequency, and M, $\mathbf{R}$, $\mathbf{V}$ and m, $\mathbf{r}^{(i)}$, $\mathbf{v}^{(i)}$ denote the mass, the position and the velocity of the $\bar{p}$ and the i-th e^+ , respectively. Although the problem appears straightforward, the strong magnetic field renders a numerical solution of the above equations quite challenging. To explore the influence of the magnetic field, we have performed two sets of simulations on different levels of sophistication.

A. Guiding center approximation

On the simplest level, the guiding center description for the e^+ dynamics, i.e. a separation of the e^+ cyclotron motion from the remaining e^+ degrees of freedom can be used. This approximation exploits that for certain strongly magnetized Rydberg states the positronic cyclotron, motion separates from the magnetron and axial bounce motion. If the cyclotron period, is the fastest period in the system, followed by the axial bounce period, and the magnetron oscillation period, ($\tau_c << \tau_z << \tau_m$), the cyclotron dynamics can be decoupled from the remaining degrees of freedom,

$$\begin{aligned} &\dot{\mathbf{r}}^{(i)} = \mathbf{v}^{(i)}\,, \\ &m v_{\mathrm{x}}^{(i)} = -\frac{F_{\mathrm{x}}^{(i)}}{\omega_{\mathrm{c}}}\,, \quad m v_{\mathrm{y}}^{(i)} = \frac{F_{\mathrm{y}}^{(i)}}{\omega_{\mathrm{c}}} \\ &m\dot{v}_x^{(i)} = F_{\mathrm{z}}^{(i)} \end{aligned} \tag{3}$$

where $\mathbf{F}^{(i)}$ is the total Coulomb force on the i-th e^+ due to the central $\bar{p}$ and the remaining e^+ . On the other hand the $\bar{p}$ cyclotron period is a factor of 1836 times longer, and must be described exactly according to Eq. 2.

B. Exact propagation of the e^+ motion

To explore the break-down of the GCA, we also follow the exact equations of motion for the e^+ , including its fast cyclotron motion. Compared to the GCA calculations, these simulations are considerably more challenging and computationally intensive; due to two major issues. First, the total simulation time is roughly six orders of magnitude longer than the cyclotron period (from a few picoseconds for the e^+ cyclotron motion to several hundreds of nanoseconds for three-body capture), which when fully resolved, would require a huge number of timesteps. Second, trajectories of deeply-bound non-GCA atoms exhibit frequent close encounters with the $\bar{p}$, making it difficult to fulfill energy conservation over the required long simulation times.

To overcome these difficulties, we used a specially designed integrator which respects the time-symmetry of the underlying Hamiltonian and exploits the disparate dynamical timescales imposed by the Coulomb and magnetic fields, respectively.

Most of the time, the $\bar{p}$ is either freely moving through the plasma, or carrying a loosely bound e^+ , such that the Coulomb interaction barely perturbs the fast cyclotron oscillations. We exploit this fact and employ a symplectic integrator, e.g., in [13], where the system Hamiltonian is split in two parts: the total Coulomb potential energy, and the total kinetic energy, including all magnetic field terms. Since this approach exactly recovers the positronic cyclotron motion, it yields high accuracy even though timesteps are chosen considerably larger than ω_c^{-1}.

For more deeply bound atoms, however, the numerical error drastically increases due to close $e^+ - \bar{p}$ encounters, requiring smaller timesteps. Adjusting the timestep accordingly, however, destroys the symplectic nature of the integrator, and results in a drift of the total energy. To circumvent this problem, we choose the binding energy of the most deeply bound e^+ as a parameter, to switch to a more suitable integrator as the e^+ gets to deeply bound levels to be accurately described by the method described above. We have tested several approaches to follow deeply bound trajectories, ranging from two-body [15] and n-body [16] regularization of the attractive e^+ - $\bar{p}$ interaction, combined with a symplectic integrator based on a triply-split Hamiltonian, to an adapted version of the time-transformed leap-frog (TTL) scheme introduced in [17]. While all of these methods gave an accurate description of the trajectories, the latter approach is conceptually more simple and was found to yield somewhat higher efficiency than the more complex regularization procedures.

The underlying idea of the TTL scheme is to introduce a scaled time $\tau = \Omega(\mathbf{R}, \mathbf{r}^{(1)}, ...)t$, but treat the scaling factor $W = \Omega$, as an independent variable. The resulting equations of motion are split into two parts

$$\frac{d}{d\tau}\begin{pmatrix}\mathbf{r}^{(i)}\\ t\\ \mathbf{v}^{(i)}\\ W\end{pmatrix} = \begin{pmatrix}\mathbf{v}/W\\ 1/W\\ (\boldsymbol{\omega}_c \times \mathbf{v}^{(i)})/W\\ 0\end{pmatrix} + \begin{pmatrix}\mathbf{0}\\ 0\\ \mathbf{f}^{(i)}/m\Omega\\ (\mathbf{v}^{(i)}/\Omega)\cdot\partial\Omega/\partial\mathbf{r}^{(i)}\end{pmatrix} \tag{4}$$

such that each part can be separately solved analytically, from which we construct a fifth order leap-frog-like integration scheme. For the scaling factor, we choose

$$\Omega = \left(\sum_i \frac{1}{\left| \mathbf{R} - \mathbf{r}^{(i)} \right|} \right)^{-1}, \tag{5}$$

which has the striking advantage that the corresponding integrator yields the exact solution for the two-body Kepler problem, in the limit of very deeply bound trajectories, where the magnetic field and the interaction with the surrounding e^+ can be regarded as a negligible perturbation. The combined integrator tracts the exact e^+ dynamics in both relevant limiting cases, i.e. for a dominating magnetic or antiprotonic Coulomb field. This ensures a highly efficient and at the same time accurate determination of the solutions of the many-body dynamics, allowing for accumulation of sufficient statistics for comparison with experiments. The solutions are themselves a valuable consistency test of the quality of the GCA.

IV. CALCULATIONS AND COMPARISON WITH OBSERVATIONS

A. Field ionization spectrum

1. Numerical results

The results of the GCA simulations, shown in Fig. 1, nicely agree with the observed low-field ionization spectrum. This suggests that the produced atoms which survive low ionizing fields are likely guiding center atoms. Indeed, the vast majority of atoms in this regime are found to exhibit the GCA hierarchy of timescales discussed above. At higher ionization fields, however, the GCA prediction for the field ionization spectrum deviates from the measured atom yield, indicating a possible break-down of the GCA approximation for more strongly bound atoms.

Our full simulations confirm the validity of the GCA for low ionization fields, but consistent with observation, deviate from it at higher ionization fields. The good agreement between the results of our full-scale calculations and the experiment, suggests that the observed deviation from the low-field power-law behavior is indeed a manifestation of deeply-bound non-GCA atoms.

2. Two-step mechanism of weakly bound states

A typical evolution of the minimal binding energy leading to a deeply bound atom is shown in Fig. 2. In accordance with previous studies [9], we find that the atomic states are changed by so-called "replacement" collisions (vertical lines in Fig.2), where the initially bound e^+ is replaced by an incident e^+ , but with a different binding energy. The e^+ is initially captured into a weakly bound orbit at a few $k_B T_{e^+}$. Subsequent thermal collisions at energies above $E_b \sim 4 k_B T_{e^+}$ − the bottleneck energy- drive the distribution

of binding energies $W(E)$ into fast equilibrium with the free plasma e^+ ,

$$W^{(\mathrm{eq})} \propto E^{-7/2} \exp\left(\frac{E}{k_\mathrm{B} T_{e^+}}\right) . \tag{6}$$

Below E_b, atoms are predominantly driven down to deeper binding and reionization is greatly suppressed [9], such that $W(E)$ strongly deviates from Eq. (6). Guided by our numerical simulations, we can determine the form of $W(E)$ below E_b. The striking feature in Fig. 2 is the prominence of a *single* replacement collision at later times, which abruptly brings the atom into a tightly-bound orbit, far removed from the thermal equilibrium. Due to the small size of the resulting atom, collisions are unlikely to significantly modify the binding energy distribution and whose dynamics can be understood in the two-step picture as an initial capture, followed by one single de-exciting collision. The rate for de-excitation at an energy E is proportional to $K(E_i, E) \propto (-E)^{-E_b/k_B T}$.

Once captured into a highly excited state with energy E_i above the bottleneck, the final energy distribution after a de-exciting event to a deeply bound state with energy $E = E_\mathrm{f}$ is thus proportional to the corresponding de-excitation rate $K(E_\mathrm{i}, E_\mathrm{f})$, which can

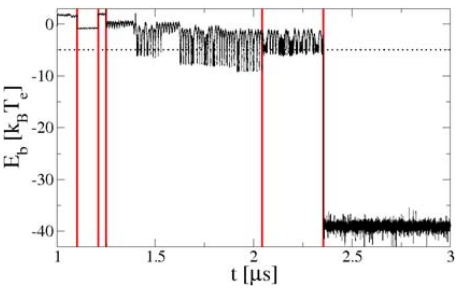

FIGURE 2. Time evolution of the minimal atomic binding, illustrating the two-step formation process. The e^+ is initially captured near the kinetic bottleneck as indicated by the horizontal dotted line. During this phase the atom undergoes a number of replacement collisions (vertical lines) until the e^+ is eventually driven down abruptly to very deep binding ($\sim -40 k_B T_{e^+}$), by a single collision near $t \sim 2.3 \mu$s..

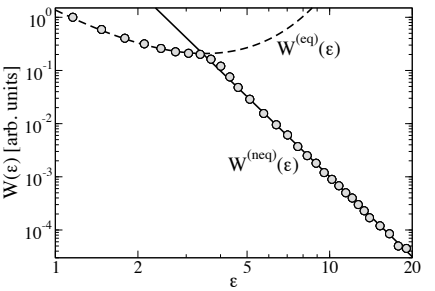

FIGURE 3. Numerically calculated binding energy distribution (dots) compared with the equilibrium distribution W_eq according to Eq.(6) (dashed line) and the power-law dependence Eq.(8) with $\varepsilon_\mathrm{b} = 4$ (solid line) arising from the two-step capture.

be obtained from [7, 9]

$$K(E_{\rm i},E_{\rm f}) = R(E_{\rm f},E_{\rm i})W_{\rm eq}(E_{\rm i})/\rho_{\rm e^+} \tag{7}$$

where $R(E_{\rm f},E_{\rm i})$ is the transition kernel for a transition between the binding energies $E_{\rm i}$ and $E_{\rm f}$. In the limits of $B = 0$ and $B \to \infty$, the energy dependence of $R(E_{\rm f},E_{\rm i})$ is well described by $R(E_{\rm f},E_{\rm i}) \propto e^{-\varepsilon_i}(-E_f)^{-(\varepsilon_{\rm b}+1)}$ [7, 9], where ε_i and $\varepsilon_{\rm b}$ denote the initial and bottleneck energies in units of $k_{\rm B}T_{e^+}$. The non-equilibrium binding energy distribution $W_{\rm neq}$ below the bottleneck hence satisfies the relation

$$W_{\rm neq}(E)dE \sim K(E_{\rm i},E)dE \propto E^{-(\varepsilon_{\rm b})}dE\ . \tag{8}$$

Our numerical binding energy distribution agrees well in Fig. 3 with this relation and the equilibrium distribution, Eq. (6), in the high and low energy regimes, respectively. Fitting Eq. (8) to the deep-binding energy tail yields $\varepsilon_{\rm b} = 4$, in nice accord with previous findings for the field-free [7] and infinite-field [9] cases.

To compare with the measured field ionization spectrum, Eq. (8) should be transformed into the corresponding distribution of maximal ionization fields, F. A one-to-one correspondence between E and F is only possible in the GCA case. As shown in [18], the maximum ionization field and binding energy of GCA atoms scale as $F \sim \rho/(\rho^2+z_{\rm m}^2)^{3/2}$ and $E_{\rm b} \propto 1/\sqrt{\rho^2+z_{\rm m}^2}$, respectively, where $z_{\rm m}$ denotes the amplitude of the axial bounce motion. Exploiting these relations, the ionization field distribution can be obtained in few straightforward steps. We first transform Eq. (8) to the spherical coordinates with the radius determined by $r = 1/E$ and subsequently to the cylindrical coordinates $(\rho, z_{\rm m})$ with $r^2 = \rho^2 + z_{\rm m}^2$, i.e.

$$W_{\rm neq}(E)dE \sim r^2 r^{\varepsilon_{\rm b}-3}dr \sim \rho\left(\rho^2+z_{\rm m}^2\right)^{\frac{\varepsilon_{\rm b}-3}{2}}dz_{\rm m}d\rho. \tag{9}$$

Transforming the arguments in the right hand side to $x = (\rho/r)^{3/2}$ and $F = \rho/r^3$ and integrating over x yields the ionization field distribution

$$P(F)dF \sim \int_0^1 \frac{x^{\frac{\varepsilon_{\rm b}+2}{3}}}{\sqrt{x^{2/3}-x^2}}dx\,F^{-\frac{\varepsilon_{\rm b}+2}{2}}dF\ . \tag{10}$$

The integral over x is well defined, so that upon integrating $P(F)$ over the ionization field F, we obtain the total number of atoms surviving a given electric field

$$N(F) \propto \int_F^\infty \tilde{F}^{-\frac{\varepsilon+2}{2}}d\tilde{F} \propto F^{-\varepsilon_{\rm b}/2}\ . \tag{11}$$

which for $\varepsilon_{\rm b} = 4$ gives $N(F) \propto F^{-2}$, as observed in the experiment [6] and in agreement with our numerical simulations.

3. Deeply-bound Rydberg states

The exact numerical scheme, outlined above, is used to search for the TBC formation of deeply-bound $\bar{\rm H}$ atoms in magnetic fields. Several such classes of atoms are shown

in Fig. 4, highlighting the differences in how these atoms ionize in experiments. Most GCA atoms form tightly in the transverse direction, but are highly elongated in the axial direction, making them susceptible to field ionization. We caution that in most theoretical treatments involving GCA [9, 13], the atoms are assume dto have negligible axial amplitude and are considered to be circular GCA atoms. The more deeply-bound atoms have, on the other hand, tight axial and transverse confinement, and although often exhibit chaotic behavior, fill a nearly spherical phase-space volume. These atoms survive large ionizing fields, resulting in a departure from the F^{-2} power-law behavior, as shown in Fig. 1.

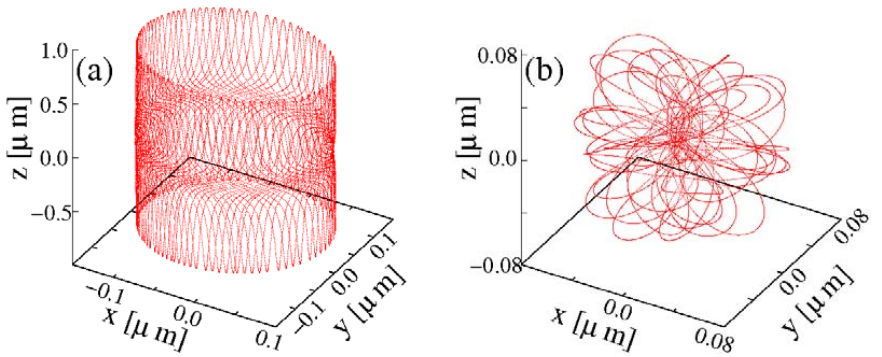

FIGURE 4. Trajectories for $\bar{H}$ atoms formed in TBC are shown depicting an elongated GCA atom (a) and a chaotic deeply-bound atom (b). From Ref. [12].

B. Velocity spectrum

The driven $\bar{H}$ production technique [3] anticipated formation of atoms with nearly thermal axial velocities, an expectation that in a later ATRAP experiment [4] was shown not to be the case. In this velocity measurement [4], the speed of $\bar{H}$ atoms was measured by adding a time-varying electric field to the existing static field, acting as a velocity selective barrier. By monitoring the fraction of atoms that passed through this oscillating field as a function of the field frequency, the ATRAP collaboration was able to deduce the characteristic velocity of the formed atoms. A monoenergetic velocity distribution $\varphi(v) = \delta(v - v_0)$ was assumed. The extracted characteristic velocity of 200 meV was found to be much larger than the thermal velocity of 0.3 meV (4.2 K).

Below, we show how charge-exchange collisions with fast $\bar{p}$ in the side wells of the nested Penning trap provide a self-consistent explanation for the observed, fast non-thermal $\bar{H}$ atoms. The TBC formed $\bar{H}$ atoms in passing through the plasma interact with the fast $\bar{p}$ ions in the side wells of the nested Penning trap; the bound positrons hop from the slow $\bar{H}$ atoms to fast $\bar{p}$ "projectiles" forming fast $\bar{H}$ atoms [12].

1. Rydberg charge exchange cross section

The Rydberg charge-exchange [19] in a magnetic field has received only little attention. Bradenbrink *et al.*[20] studied the electron transfer from Rydberg atoms in collision with singly-charged ions in a laboratory magnetic field. The initial state was chosen from a stationary microcanonical ensemble corresponding to a fixed binding energy.

Here, we calculate the charge exchange cross section for each microscopic internal and translational atomic state, produced by the preceding Monte-Carlo simulation to describe the initial formation of $\bar{\mathrm{H}}$. By firing a large number $\bar{p}$ of varying incident energy onto the TBC $\bar{\mathrm{H}}$ atoms, we obtain the cross section for charge exchange for each microscopic initial state. The initial and final states of the $\bar{\mathrm{H}}$ atoms are labeled by the maximum surviving fields, F_{i} and F_{f}, such that the state-selective cross section $\sigma_{\mathrm{cx}}(F_{\mathrm{i}}, F_{\mathrm{f}}; v_{\bar{H}}, v_{\bar{p}})$ for charge exchange between an incident $\bar{p}$ with velocity $v_{\bar{p}}$ and an $\bar{\mathrm{H}}$ with velocity $v_{\bar{H}}$ ionizing at a maximum field F_{i} can be defined. The resulting $\bar{\mathrm{H}}$ atom moving at $v_{\bar{p}}$ will ionize at a maximum field F_{f}. Since the charge exchange depends only on the relative velocity between the projectile and the initial TBC atom, and $v_{\bar{p}} \gg v_{\bar{H}}$, the resulting cross sections are nearly independent of $v_{\bar{H}}$.

In Fig. 6, we show the average total capture cross section $\bar{\sigma}_{\mathrm{cx}}(F_{\mathrm{i}}, v_{\bar{p}}) = \int \sigma_{\mathrm{cx}}(F_{\mathrm{i}}, F_{\mathrm{f}}; v_{\bar{p}}) dF_{\mathrm{f}}$ as a function of $v_{\bar{p}}$ for different F_{i}. As expected, the cross sections are very large and quickly drop as the relative collision velocity increases. The cross section maxima are due to a matching of Rydberg e^+ and $\bar{p}$ velocities [19].

2. Charge exchange influence on detection

The probability for charge exchange as the initially slow $\bar{\mathrm{H}}$ atoms move through the $\bar{p}$ plasma in the side wells is obtained from

$$P_{\mathrm{cx}}(F_{\mathrm{i}}, F_{\mathrm{f}}; v_{\bar{p}}, v_{\bar{H}}) = 1 - \exp\left(-\sigma_{ex} n_{\bar{p}} d \frac{v_{\bar{p}}}{v_{\bar{H}}}\right) , \tag{12}$$

where $n_{\bar{p}}$ and d denotes the density and the length of the $\bar{p}$ plasma in the side wells of the nested Penning trap and the $\bar{\mathrm{H}}$ travel time through the $\bar{p}$ cloud is $d/v_{\bar{H}}$.

Despite the large cross sections, Eq. (12) yields small exchange probabilities for typical experimental values. The ATRAP experiments, however, only detect atoms within a small opening angle $2\pi\alpha$ along the magnetic field direction, such that the corresponding detection efficiency $\kappa(v, \alpha)$ strongly depends on the atomic velocity v and hence can strongly be influenced by charge exchange collisions. Assuming free motion of the produced atoms, the transverse thermal diffusion gives a detection efficiency,

$$\kappa(v, \alpha) = 1 - \exp\left(-\frac{mv^2}{2k_B T_\perp} \frac{\alpha}{\pi}\right) , \tag{13}$$

where we assumed a transverse $\bar{\mathrm{H}}$ temperature ($T_\perp = T_{e^+}$). Fig. 5 shows the detection efficiency κ as a function of the $\bar{\mathrm{H}}$ kinetic energy. Fast $\bar{\mathrm{H}}$ produced by charge exchange are detected with practically 100% efficiency while κ quickly drops as the $\bar{\mathrm{H}}$ velocity decreases.

With $N(F)$ being the number of initially formed $\bar{\mathrm{H}}$ that survive a given field F, the fraction of detected slow $\bar{\mathrm{H}}$ atoms that do not charge exchange, after traversing the side well, is given by

$$f_{\mathrm{ncx}}(F,v) = N(F)\kappa(\alpha,v)\phi_{\bar{H}}(v)\int \phi_{\bar{p}}(v_{\bar{p}})\left[1 - P_{\mathrm{cx}}\left(F,F_{\mathrm{f}};v_{\bar{p}},v\right)\right] dF_{\mathrm{f}}d^3v_{\bar{p}}\ , \tag{14}$$

while the fraction of detected fast $\bar{\mathrm{H}}$ produced by charge exchange collisions is obtained from

$$f_{\mathrm{cx}}(F,v) = \phi_{\bar{p}}(v)\int N(F_{\mathrm{i}})\phi_{\bar{H}}(v_{\bar{H}})P_{\mathrm{cx}}(F_{\mathrm{i}},F;v,v_{\bar{H}})dF_{\mathrm{i}}d^3v_{\bar{H}}\ , \tag{15}$$

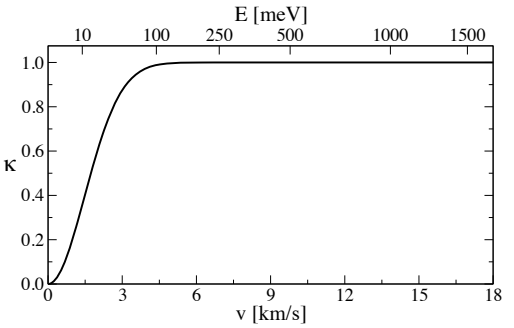

FIGURE 5. Detection efficiency $\kappa(v,\alpha)$ as a function of the velocity v of the detected $\bar{\mathrm{H}}$ atom, and for $\alpha = 4\pi/250$.

3. Charge-exchange influence on $\bar{\mathrm{H}}$ *field ionization*

Let us first examine the influence of charge exchange collisions on the field ionization spectrum discussed previously. The average number of slow and fast atoms – those that undergo charge exchange, as a function of the initial $\bar{\mathrm{H}}$ velocity, is obtained from

$$\bar{f}_{\mathrm{ncx}} = \kappa(\alpha,v_{\bar{H}})\left[1 - \int \phi_{\bar{p}}(v_{\bar{p}})P_{\mathrm{cx}}\left(F_{\mathrm{i}},F_{\mathrm{f}};v_{\bar{p}},v_{\bar{H}}\right)dF_{\mathrm{f}}d^3v_{\bar{p}}\right]\ , \tag{16}$$

and

$$\bar{f}_{\mathrm{cx}} = \int \kappa(\alpha,v_{\bar{p}})\phi_{\bar{p}}(v_{\bar{p}})P_{\mathrm{cx}}\left(F_{\mathrm{i}},F_{\mathrm{f}};v_{\bar{p}},v_{\bar{H}}\right)dF_{\mathrm{f}}d^3v_{\bar{p}}\ , \tag{17}$$

The resulting fraction of fast atoms, $\bar{f}_{\mathrm{cx}}/(\bar{f}_{\mathrm{cx}} + \bar{f}_{\mathrm{ncx}})$, is shown in Fig. 6(b) as a function of the kinetic energy $E_{\bar{H}} = Mv'^2/2$ of the slow initially formed atoms, for different ionizing electric fields. The fraction is nearly independent of the electric field, such that the field ionization spectrum remains unaffected by charge exchange collisions. In other words, our findings discussed in the preceding sections also apply when charge-exchange collisions are included. This point is illustrated in Fig. 7, where we show the field spectrum for atoms surviving an electric field before and after charge exchange.

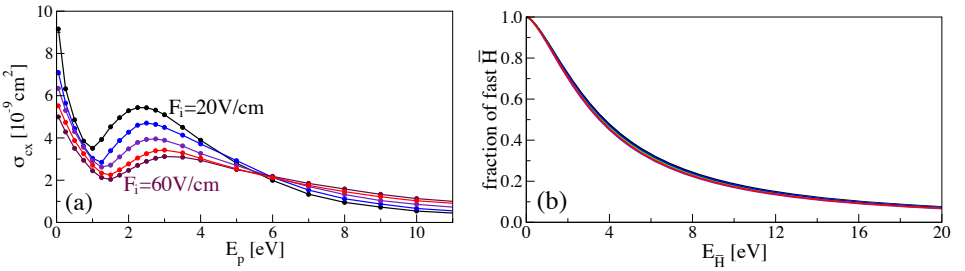

FIGURE 6. e^+ exchange cross section from 1 meV $\bar{H}$ atoms as a function of $\bar{p}$ axial energy, for different ionization fields in the range, 20 – 60 V/cm.

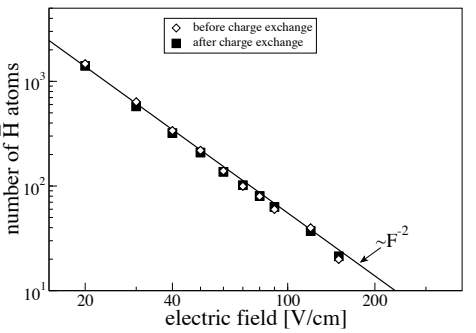

FIGURE 7. Comparison of the field ionization spectrum, calculated within the GCA, before (open diamonds) and after (filled squares) charge exchange.

4. Charge exchange effect on $\bar{H}$ *velocity distribution*

The velocity distribution of the atoms that reach the detector is obtained by adding the contributions from the slow (fast) atoms that do not (do) charge exchange, as given by Eqs. (14) and (15) and integrate over the ionization field

$$\phi(v) = \int f_{ncx}(F,v) + f_{cx}(F,v)dF \tag{18}$$

The exact initial velocity distributions $\phi_{\bar{p}}$ and $\phi_{\bar{H}}$ are not known. Here, we assume Gaussian distributions with temperatures $T_{\bar{H}}$ and $T_{\bar{p}}$, respectively.

The characteristic energy of the high-energy $\bar{p}$ is determined by the depth of the side-wells, which is about 10 eV. The exact form of the $\bar{p}$ axial velocity distribution is not important for obtaining the $\bar{H}$ final velocity distribution, since the charge exchange cross sections (Fig. 6) decrease quickly above projectile energies above several eV. The temperature $T_{\bar{H}}$ of the initially formed $\bar{H}$, on the other hand, is determined by comparing the resulting field ionization spectrum with the experimental observation. As shown in Fig.8, our calculated spectra agree with the experimental data for temperatures ranging from 1 meV to 10 meV – considerably smaller values than one would extract

by including charge exchange collisions.

The effect of charge exchange collisions is further illustrated in Fig. 8b, where we show the calculated velocity distribution of $\bar{H}$ atoms arriving at the detector. The low-velocity peaks are due to the slow, initially formed, $\bar{H}$ atoms that do not charge exchange, i. e. $\phi_{\bar{H}}$. The extended plateau at larger velocities arises from charge exchange with the fast $\bar{p}$ atoms in the side wells. The latter produces the high-frequency tail in the observed field spectrum.

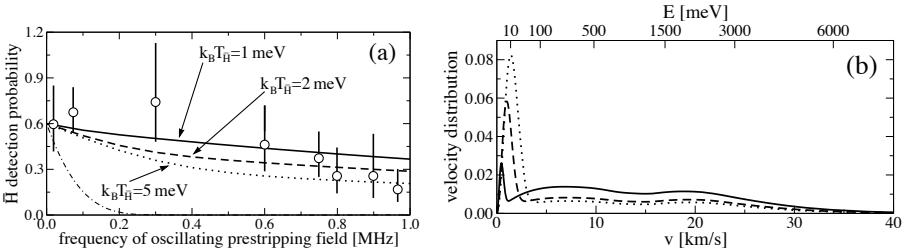

FIGURE 8. (a) Proposed charge exchange mechanism produces a frequency dependent field ionization spectrum consistent with experimental data [4] (circles). The spectra have been calculated for $k_BT_{\bar{p}} = 8$eV and $k_BT_{\bar{H}} = 1$meV (solid line), $k_BT_{\bar{H}} = 2$ meV (dashed line) and $k_BT_{\bar{H}} = 5$meV (dotted line). The dot-dashed line shows the spectrum that results by neglecting e^+ charge transfer for $kT_{\bar{H}} = 2$meV ($T_{\bar{H}} = 30$K). (b) Corresponding velocity distributions after charge exchange. From Ref. [12]

V. SUMMARY

We present classical Monte Carlo simulations that explain several observations of previous ATRAP $\bar{H}$ experiments. It is found that the formation of guiding center atoms at low ionizing fields is responsible for the F^{-2} dependence of observed field ionization spectrum, allowing for an analytical verification of the numerical results. Deviations from this power-law at higher ionization fields, occurring in the Monte-Carlo simulations and observed experimentally, can be attributed to the formation of non-guiding center atoms. It is further demonstrated that an auxiliary formation mechanism, particular to nested Penning traps, is responsible for producing fast non-thermal $\bar{H}$ atoms. This mechanism, the charge exchange with fast $\bar{p}$ projectiles in the side wells, yields field ionization spectra in agreement with the experiment and suggest that $\bar{H}$ atoms much slower than detected are produced.

VI. ACKNOWLEDGEMENT

This work was supported by NSF through a grant for ITAMP at Harvard University and Smithsonian Astrophysical Observatory.

REFERENCES

1. M. Amoretti *et al.*, Nature **419**, 456 (2002).

2. G. Gabrielse *et al*., Phys. Rev. Lett. **89**, 213401 (2002).
3. G. Gabrielse *et al*., Phys. Rev. Lett. **89**, 233401 (2002).
4. G. Gabrielse *et al*., Phys. Rev. Lett. **93**, 073401 (2004).
5. M. Amoretti *et al*., Phys. Lett. B **583**, 59(2004).
6. G. Gabrielse, Ad. At. Mol. Opt. Phys. **50**, 155(2005).
7. P. Mansbach and J. Keck, Phys. Rev. **181**, 275(1969).
8. F. Robicheaux and J. D. Hanson, Phys. Rev. A **69**, 010701(R) (2004).
9. M. Glinsky and T. O'Neil, Phys. Fluids **B 3**, 1279(1991)
10. S. X. Hu, D. Vrinceanu, S. Mazevet, and L. A. Collins Phys. Rev. Lett. **95**, 163402 (2005).
11. F. Robicheaux, Phys. Rev. A **70**, 022510 (2004).
12. T. Pohl, H. R. Sadeghpour, and G. Gabrielse, Phys. Rev. Lett. **97**, 143401 (2006).
13. D. Vrinceanu *et al*., Phys. Rev. Lett. **92**, 133402 (2004).
14. F. Driscoll, Phys. Rev. Lett. **92**, 149303 (2004).
15. G. D. Quinlan and L. Hernquist, New Astron. **2**, 533(1997).
16. C. D. Heggie, Celest. Mech. **10**, 217(1974).
17. S. Mikkola and S. Aarseth, Celest. Mech. & Dyn. Astron. **84**, 343(2002).
18. S.G. Kuzmin and T.M. O'Neil Phys. Plas. **12**, 012101 (2005).
19. D. M. Homan *et al*., Phys. Rev. A **58**, 4565 (1998); K. B. MacAdam *et al*., Phys. Rev. Lett. **75**, 1723 (1995); V. N. Ostrovsky, J. Phys. B: **28**, 3901 (1995).
20. S. Bradenbrink *et al*., J. Phys. B: **30**, L161 (1997).